Journal of Energy Storage 133 (2025) 117841

Contents lists available at ScienceDirect

Journal of Energy Storage

journal homepage: www.elsevier.com/locate/est

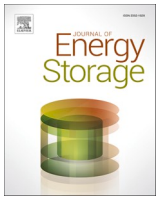

Research papers

Experimental characterization of a vertical shell-and-tube latent heat thermal energy storage with dual-tube finned tubes for evaporation at temperatures about 133 °C

K. Theologou, L. Dietz, J. Tombrink, M. Johnson *

Institute of Engineering Thermodynamics, German Aerospace Center (DLR), Pfaffenwaldring 38-40, 70569 Stuttgart, Germany

ARTICLE INFO

Keywords:
Phase change material (PCM)
Dual-tube heat exchanger
Extruded longitudinal aluminium fins
Passive discharging process
R1233zd(E) evaporation
Process heat/steam

ABSTRACT

Significant progress has been made in the development of latent heat thermal energy storage technologies for process industry and power plant sector applications, and storage systems in the megawatt range have been demonstrated on a pilot scale. Cost-effective storage materials have low thermal conductivities, and a central task in the realization of economical storage technologies is to find cost-effective solutions for heat transfer during the charging and discharging process. In the current state of the art, parallel tube heat exchangers with finned tubes are integrated into the storage material. This publication describes a modified storage unit in which a vertical shell-and-tube type heat exchanger with a novel dual-tube finned tube design is used to enable charging and discharging with different working fluids by condensing and evaporating them. This can increase the efficiency of the storage process and simplify the overall system by reducing integration equipment needs. The focus here is on the experimental characterization of the discharging process of the latent heat thermal energy storage, showing data from experiments with a mixture of potassium nitrate and lithium nitrate (KNO_3-$LiNO_3$) as the phase change material with a phase change temperature of about 133 °C and R1233zd(E) as the heat transfer fluid. An extensive parameter study was carried out to investigate the transient heat flow rate profile and temperature distribution in the storage, as well as the corresponding outlet condition under rarely-reported non-nominal conditions. The results show that the latent heat thermal energy storage is capable of storing up to 124 kWh of heat in a temperature range of 104 to 139 °C with a maximum heat flow rate of up to 90 kW. Furthermore, it is shown that the maximum heat flow rate, the duration of a constant heat flow rate and superheating can be controlled by adjusting the mass flow rate. The outcomes of this study contribute to improved design and operating strategies for future passive latent heat storage technologies and can serve for numerical model validation.

1. Introduction

The increasing integration of renewable energies into the electricity grid underscores the urgent need for effective solutions for energy storage, given the fluctuations in renewable energy generation [1–3]. For processes using steam as the working fluid, latent heat thermal energy storage (LH-TES) enables solutions with high volumetric heat storage capacity, steam supply at almost constant conditions and high exergetic efficiencies, as the charging and discharging processes take place in narrow temperature intervals and thus correspond to the temperature profile of the evaporation and condensation processes. LH-TES have been developed for application in the process industry and in the power plant sector [4,5], and storage systems in and near the megawatt range have been demonstrated at a pilot scale [5,6].

An emerging application area for LH-TES are thermo-mechanical storage concepts based on a combination of Rankine cycles and heat storage units where the LH-TES is charged by a process similar to a heat pump [7]. During discharge, the heat stored is used to operate a steam cycle. Here, compressed heat energy storage (CHEST) is one concept using LH-TES to increase efficiency by minimizing the temperature differences between the working fluid and the storage medium during the evaporation and condensation processes, according to Steinmann [8]. The CHEST concept also falls under the umbrella of Carnot battery and pumped thermal energy storage, described by Vecchi et al. [9] and Dumont et al. [10].

* Corresponding author.
E-mail address: Maike.Johnson@dlr.de (M. Johnson).

https://doi.org/10.1016/j.est.2025.117841
Received 28 December 2024; Received in revised form 12 June 2025; Accepted 21 July 2025
Available online 8 August 2025

Nomenclature

Variables

$\bar{c}_p$	isobaric heat capacity [J/(kgK)]
dur	duration [h]
h	specific enthalpy [kJ/kg]
$\dot{m}$	mass flow rate [kg/s]
p	pressure [bar]
$\dot{Q}$	heat flow rate [W]
Q	heat [kWh]
T	temperature [°C] or [K]
t	data acquisition time [s]
$\dot{V}$	volumetric flow rate [m^3/h]
ε	relative error [%]
σ	absolute error [ ]
ϱ	density [kg/m^3]

Subscripts

am	ambient
bot	bottom
C	charging process
con	condenser
edge	edge
D	discharging process
LH	LH-TES
in	inlet
ini	initial conditions
i	time period
j, k	variables
max	maximum
mean	arithmetic mean
n	number of time periods
oil	oil
out	outlet
ref	refrigerant
sens	sensible heat transfer
top	top

Abbreviations

CHEST(ER)	compressed heat energy storage (for Energy from Renewable Sources)
DLR	German Aerospace Center
DSC	direct scanning calorimetry
Exp.	experiment
HT-HP	high-temperature heat pump
LH-TES	latent heat thermal energy storage
ORC	organic Rankine cycle
PCM	phase change materials
TS	test series
V	valve

Various storage design concepts have been developed and researched for medium and high-temperature thermal energy storage [11,12]. These can be divided into active [13] and passive [14] storage concepts. For this storage system, a passive concept has been further developed. A common design for passive LH-TES is based on parallel tube heat exchangers immersed in the phase change material (PCM) in the form of a shell-and-tube heat exchanger. This design enables simple and cost-effective pressure-vessel design on the evaporation and condensation side by adjusting the tube diameter and tube wall thickness [15]. In addition, variation of the number and length of the heat exchanger tubes allow for scalability. Nevertheless, enhancing heat transfer in the PCM with low thermal conductivity is one of the critical aspects. Numerous techniques have been developed to overcome the problem of the low PCM thermal conductivity. Choure et al. [16] reviewed heat transfer techniques for PCMs and summarised that using fins to extend the heat transfer surface is the most common way for tube-based heat exchangers, due to low cost and simplicity in usage as well as the freedom in shape design. In their review, Zhang et al. [17] focus on the prospective fin design for heat transfer enhancement in the PCM. They found that most of the fin designs investigated in literature are annular and longitudinal, with the latter focusing on PCM melting and thus on the LH-TES charging process. An overview of vertically orientated experimental shell-and-tube LH-TES with annular and longitudinal aluminium fins is given in Table 1. A numerical study by Ren et al. [18] found that a vertical snowflake longitudinal fin can significantly shorten the charging time of the LH-TES in comparison to annular fin designs. Similar types of vertical longitudinal fins based on extruded aluminium profiles were developed and experimentally tested in a lab-scale PCM storage module by Laing et al. [19], with the potential of cost reduction of the finned-tube concept and a large freedom in LH-TES design concerning storage performance through variation of fin diameter and shape. Vogel et al. [20] developed a simplified model allowing for the design of vertical large-scale LH-TES based on longitudinal snowflake fins. Johnson et al. [21] designed an LH-TES with such fins, which was later assembled and experimentally tested [5]. To this end, Johnson et al. [22] previously studied an assembly and attachment method for extended aluminium fins onto steel tubes. The review from Low et al. [14], which deals with fins in LH-TES, analyses the influence of different

Table 1
Examples of vertically orientated experimental shell-and-tube LH-TES with annular and longitudinal aluminium fins at medium and high temperatures.

Reference	Location	PCM (mass)	Phase change temperature	Heat transfer fluid	Number of tubes (length)	Fin type	Rated heat flow rate	Storage capacity
Laing et al.	Carboneras (Spain)	$NaNO_3$, (14,000 kg)	306 °C	water/steam	152 (6 m)	Annular	200 kW_{th}	700 kWh_{th}
Couvreur et al.	Ghent (Belgium)	KNO_3-$NaNO_3$, (3637 kg)	222 °C	thermal oil	36 (5.5 m)	Annular	50–150 kW	220 kWh_{th}
Garcia et al.	Grenoble (France)	$NaNO_3$, (6300 kg)	306 °C	water/steam	61 (n.a.)	Annular with longitudinal inserts	50 kW_{th}	380 kWh_{th}
Vuillerme et al.	Cadarache (France)	$NaNO_3$, (18,000 kg)	306 °C	water/steam	61 (4.5 m)	Annular with longitudinal inserts	150 kW_{th}	852 kWh_{th}
Laing et al.	Stuttgart (Germany)	$NaNO_3$, (320 kg)	306 °C	thermal oil	7 (1 m)	Longitudinal	5 kW_{th}	15 kWh_{th}
Johnson et al.	Stuttgart (Germany)	$NaNO_3$, (1375 kg)	306 °C	thermal oil	18 (1 m)	Longitudinal	7 kW_{th}	70 kWh_{th}
Johnson et al.	Saarland (Germany)	$NaNO_3$, (32,000 kg)	306 °C	water/steam	852 (5.6 m)	Longitudinal	6000 kW_{th}	1500 kWh_{th}

fin parameters on the PCM dead zones and suggests that future research should investigate the partial charging and discharging of LH-TES as well as methods for maintaining the discharge rate and temperature for reliable operation. Partial charging would possibly occur when charging using renewable energy sources. Partial discharging, on the other hand, would possibly occur with a storage integrated into an industrial process coupling batch processes in which discharge capacities and times vary, for example due to differing curing times in autoclaves.

The majority of passive LH-TES in once-through operation for steam generation have been operated either at a constant pressure, which results in a decreasing steam mass flow rate with constant steam pressure and temperature, or at sliding pressure and consequently at a constant steam mass flow rate with decreasing pressure and temperature [19,23]. Optimised operating strategies with a strong focus on control of the mass flow rate and pressure of the steam flow for delivering steam with constant mass flow rate, pressure and temperature have only emerged in recent years, as described by Garcia and Largiller, based on experiments, and by Dietz et al. [24] with help of analytical and numerical simulations. Garcia and Largiller [25] analyse the actual heat flow rate profile of the LH-TES while Dietz et al. [24] studies the physical processes and describes these in more detail to deepen understanding and derive more complex operating strategies. These authors agree that the variation of the mass flow rate in fixed pressure operation can be used to regulate the dominant heat transfer surface and thus the heat flow rate of the LH-TES during the duration of the discharging process. Furthermore, Dietz et al. numerically demonstrates the influence of the mass flow rate variation on the temperature stratification in the LH-TES. Increasing the mass flow rate of the heat transfer fluid results in increasing the dominant heat transfer surface, thus increasing the heat flow rate and decreasing the temperature stratification in the LH-TES. This leads to a decreasing discharging process duration.

Within the framework of the H2020 project CHESTER [26], the world's first laboratory-scale prototype of a Rankine-based Carnot battery for sector coupling at a representative scale of 10 kW_{el} was developed, constructed, and experimentally tested [27]. In the CHESTER prototype, two working fluids are required for the charging and discharging processes for the specific choice of the high-temperature heat pump (HT-HP) with R1233zd(E) described by Ramirez et al. and the organic Rankine cycle (ORC) engine with R1336mzz(E) described by Couvreur et al. [28]. As part of the high temperature thermal energy storage system, a novel vertical shell-and-tube LH-TES with dual-tube finned tubes, separating the charging and discharging cycles, was developed, designed and constructed. This system design allows for direct heat exchange into the storage system, thereby minimizing system temperature gradients. Another possibility would have been to have a closed-loop system, connecting to the HT-HP and ORC via heat exchangers. This would have significantly increased the said temperature gradients, decreasing overall system efficiency. This dual-tube concept is also thought to be useful for industrial process heat applications in which different working fluids are used for the charging and discharging processes, e.g. feedwater and condensate or thermal oil and water, or significantly different pressure levels for the charging and discharging medium.

This publication presents a vertical shell-and-tube LH-TES with a novel design of extruded longitudinal aluminium fins and discusses the operation experience herewith. The storage is investigated and characterised and insights into possible operation strategies are given. The focus is on PCM solidification and thus the discharging process, as the heat demand in industrial processes is often more critical than the supply for charging. As there are integrations in which the charging process is also or more critical – i.e. the CHESTER system for which this storage was designed – future work will analyse the charging processes as well. Furthermore, this paper analyses the case of interrupted discharging of the storage with breaks between the discharging stages.

2. Experimental setup

2.1. Latent heat thermal energy storage

This publication analyses the influence of various parameters on the LH-TES discharging process concerning the heat flow rate and temperature distribution in the PCM. Fig. 1 shows a 3D-drawing of the LH-TES, which was designed as part of the high temperature thermal energy storage system in the CHESTER prototype described in more detail in [27]. The outer shell of the LH-TES is a rectangular containment with an inner volume of 1000 × 1070 × 3000 mm^3. Including the base, the total LH-TES height is 4647 mm. The boundary conditions were defined by the thermal and thermodynamic conditions of the HT-HP, with approximate heat flow rates of 30 kW_{th} for the charging process, and of the ORC, with approximate heat flow rates of 43 kW_{th} for the discharging process. The LH-TES capacity was designed to allow for a complete charging and discharging cycle within one day. For the detailed design, a thermodynamic analysis of the internal heat exchanger and a parameter study to determine the required LH-TES configuration were carried out similar to Johnson et al. [21].

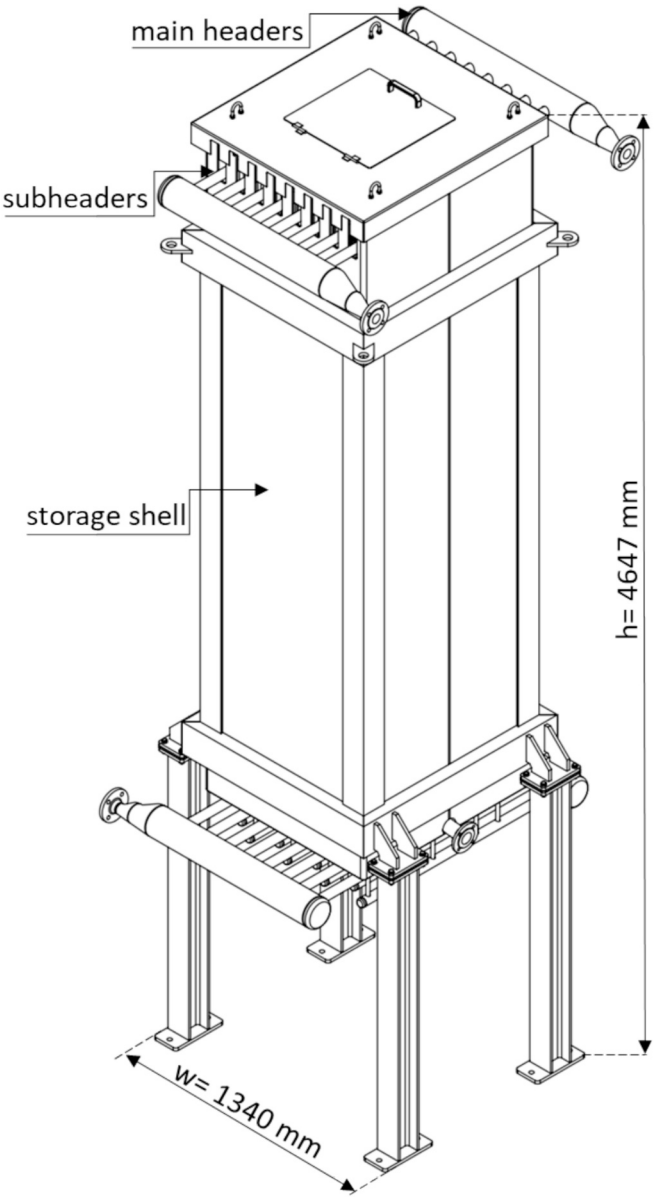

Fig. 1. Technical drawing of the LH-TES.

Due to the use of two different refrigerants and lubricants for the HT-HP and ORC circuits, the LH-TES was designed and built as a dual-tube vertical shell-and-tube type. The dual-tube design enables the utilisation of different fluids and operating pressures in the tubes, thus increasing the flexibility and efficiency of the LH-TES in terms of integration and operation. For example, in an industrial process, water can be used to generate process steam in one tube register for the discharging process and a suitable refrigerant can be used in the second tube register for the charging process. Furthermore, stress and damage to the tubes due to large and rapid fluctuations in pressure and temperature when switching between charging and discharging can be avoided. On the fluid side, the vertical orientation of the tubes allows the vaporising fluid to flow upwards along the density gradient during the charging process, while the condensing fluid flows downwards using the gravitational force during the discharging process. On the PCM side, liquefaction occurs from top to bottom of the LH-TES during the charging process. This reduces mechanical stresses on the LH-TES shell and on the tubes due to volumetric expansion of the PCM, while solidification occurs from bottom to top during the discharging process [20].

The two tube registers are thermally and physically connected by aluminium fins, as depicted in Fig. 2. To ensure a high heat output while minimizing the temperature difference between the phase change material (PCM) and the refrigerant, heat transfer structures made of extruded longitudinal aluminium fins were developed through an iterative process in collaboration with a manufacturer, considering techno-economic and feasibility factors. The extruded 3 m-long fin halves made of the aluminium alloy 6060 are affixed to the tubes using 1.4310 spring steel clips. The hexagonal configuration of the fin-pair structure has an approximate outer diameter of 139 mm and an approximate fin volume fraction of 18 %. Further details regarding the attachment method can be found in Johnson et al. [22]. In total, 56 finned-tube pairs are inserted in the LH-TES, whereby each tube has an outer diameter of 17.3 mm and a wall thickness of 2.3 mm. The tube-pairs are aligned in rows of seven by eight and the rows of seven are connected to two sub-header sets, each with an outer diameter of 42.4 mm and a wall thickness of 3.0 mm. The tube-pair arrangements and header alignments are shown in Fig. 4, along with the thermocouples discussed in that section. The resulting eight pairs of sub-headers are connected to two main headers, each with an outer diameter of 139.7 mm and a 4.0 mm wall thickness. The material used for the tubes and outer shell of the LH-TES is 16Mo3. A 100 mm thick layer of mineral wool serves as thermal insulation of the LH-TES.

For the choice of the PCM, the limitations of the available HT-HPs required for the development of the CHESTER prototype led to an upper limit for the melting temperature of the PCM of 160 °C [29]. Based on data given by Guizane et al. [30] and Tamme et al. [31], the eutectic mixture of KNO_3 and $LiKNO_3$ with a theoretical phase change temperature of 133 °C and a PCM mixing ratio of 67 wt% KNO_3 and 33 wt% $LiNO_3$ was chosen, with a fill weight of approximately 4450 kg. However, during the commissioning phase, it was observed that the PCM exhibited phase change behaviour in a temperature range of approximately 128 to 136 °C, indicating that the intended eutectic mixture was not achieved. This discrepancy may be due to improper mixing procedures or inaccuracies in the literature data. Roget et al. showed in their study that the composition of the eutectic mixture of KNO_3 and $LiNO_3$ reported in the literature is inconsistent and scattered. For the specific phase change enthalpy values of 160 and 170 kJ/kg and for the specific isobaric heat capacity 1.17 kJ/(kgK) are stated in Milian et al. [32]. DLR-in house measurements confirm this order of magnitude.

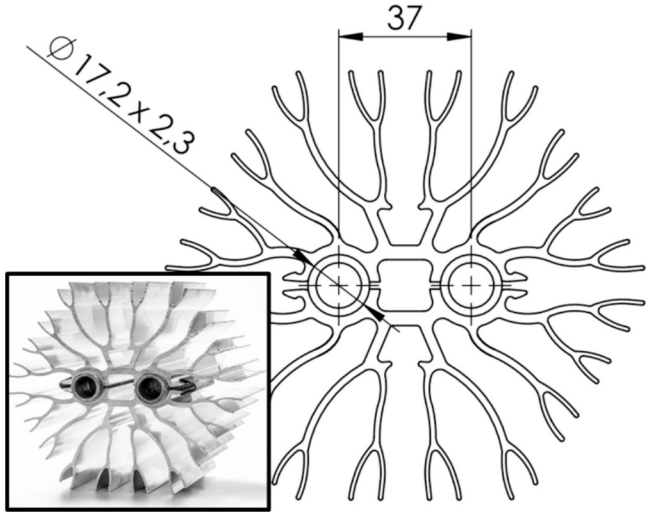

Fig. 2. Dual-tube finned tube design for the LH-TES.

2.2. Test rig

The LH-TES, although designed for operation in the CHESTER system, was additionally characterised using a separate test rig for detailed analysis on the component level. Results of the operation of the LH-TES as part of the high temperature thermal energy storage system and its interaction with the other components of the CHESTER prototype can be found in Theologou et al. [27]. The independent testing rig is a vapour generation test facility, which was also used in the CHESTER prototype operation for preconditioning the LH-TES. This rig can be operated with various fluids, whose properties determine the permitted operating conditions. For the experiments discussed here, the refrigerant R1233zd (E) with a critical pressure of 36.2 bar and a critical temperature of 166.5 °C was used [33]. The heating capacity was provided by a 100 kW electric heater and the cooling capacity by the in-house cooling water network with 150 kW at 15 °C. For the chosen refrigerant, the evaporation temperature is limited to 145 °C and the operating pressure to 40 bar.

Fig. 3 shows a simplified flow diagram of the test rig, with each pipe colour representing a specific working fluid in the four circuits. Controlled with the valves V1-V5 in the primary circuit, the system can charge and discharge the LH-TES, with a rig-internal regulation of the refrigerant to achieve the desired temperature.

During the charging process (grey arrows), valves V1, V2 and V5 are open, while V3 and V4 are closed. The refrigerant is conditioned as it flows through the feed pump, the preheater, the evaporator and the superheater. Initially, the refrigerant enters the LH-TES from above in a gaseous state and leaves it from below in either a two-phase or liquid state. The refrigerant is then condensed and subcooled in a condenser and a subcooler to achieve a liquid state before entering the feed pump again.

During the discharging process (shown with purple arrows), valves V3 and V4 are open, while V1, V2 and V5 are closed. Downstream of the feed pump, the refrigerant flows through the preheater while still in a liquid state and enters the LH-TES from below. Flowing through the LH-TES, the refrigerant vaporises and changes from a liquid to a gaseous or two-phase state. After leaving the LH-TES and flowing back to the test facility, it is liquefied again by the condenser and the subcooler. Due to the control mechanisms, the mass flow rate varies during the charging process while remaining nearly constant with only slight fluctuations during the discharging process. The system pressure results mainly from the setpoint temperature in the condenser.

2.3. Measurements and measurement accuracy

The simplified piping and instrumentation diagram in Fig. 3 shows the measuring points and valves relevant to the following analysis. Table 2 lists all measuring sensors and devices whose values were used for the data reduction.

The mass flow rates of the refrigerant are measured using Coriolis

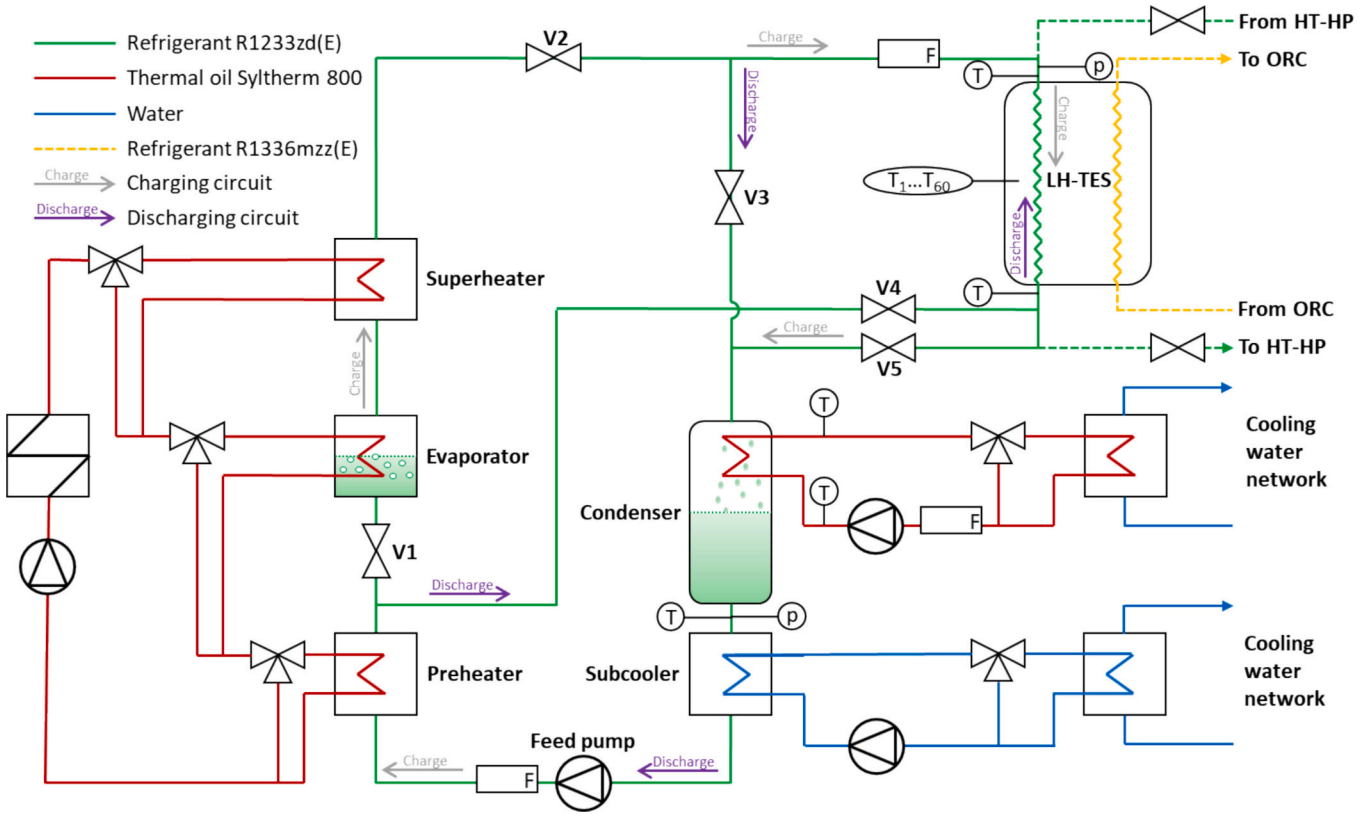

Fig. 3. Simplified piping and instrumentation-diagram of the test rig.

Table 2
Measurement devices and their accuracy.

Parameter	Sensor	Manufacturer/type	Accuracy
refrigerant mass flow rate charging	Coriolis mass flow meter	Krohne, OPTIMASS 6000 – S 25 with MFC 400 F	$\pm(0.0005 \cdot \dot{m})$
refrigerant mass flow rate discharging	Coriolis mass flow meter	Heinrichs, TME-S40 with UCM4	$\pm(3 + 0.001 \cdot \dot{m})$ kg/h
oil volumetric flow rate	vortex flow meter	ABB, VortexMaster FSV430	$\pm(0.01\ \% \cdot \dot{V})$
refrigerant pressure LH-TES	piezoresistive absolute pressure transmitter	Endress + Hauser GmbH+Co. KG, Cerabar SPMC71, (0…40 bar)	0.05 % FS, ±20 mbar
refrigerant pressure condenser	piezoresistive absolute pressure transmitter	Aplisens, PCE-28. Smart, (0…70 bar)	0.1 % FS, ±70 mbar
refrigerant temperature	PT100 RTD, 4-wire	KMP, spring fixed sheath sensor in immersion sleeves	1/10 Class B, $\pm(0.3\ °C + 0.005 \cdot T)$/10
oil and condenser temperature	PT100 RDT, 3-wire	Electrotherm	Class A, $\pm(0.15\ °C + 0.002 \cdot T)$
PCM temperature	type K multipoint-sheath-Thermocouples	ES Electronic Sensor GmbH, (6xIKT05/0-2500/2KTT/6m)	Class 1, ±1.5 °C

mass flow meters. For the charging process, the mass flow meter is installed after the superheater. During the discharging process, the mass flow rate is downstream of the feed pump. The volumetric flow rate in the thermal oil circuit between the condenser and the cooling water network is measured with a vortex flow meter. One pressure sensor is installed on the top of the LH-TES, approximately 100 mm next to the temperature measurement past the flanges of the upper main header to measure the refrigerant. At the top and the bottom of the LH-TES, the temperature sensors are mounted approximately 200 mm from the flanges of the main headers within a weld-in protective sleeve with a diameter of 20 mm, which tapers to 10 mm towards the measuring tip and protrudes approximately halfway into the cross-section of the tube. For the temperature measurement at the condenser outlet, the thermal oil inlet and outlet temperature sensors were integrated directly into the flow.

To investigate the temperature distribution in the LH-TES, 10 multipoint thermocouples with six measurement levels each were placed at different horizontal positions in the PCM to provide a measurement at six heights, while ensuring measurement in the same position at these different heights. In addition, the use of multipoint thermocouples reduces the disturbances to the system by having only one object introduced for each of the six measurements. Fig. 4 shows the multipoint thermocouples labelled with "X" in a horizontal cross-sectional view of the LH-TES. The multipoint thermocouples located in the finned area of the tubes are labelled in red and a multipoint thermocouple at the edge of the LH-TES in the fin-free area, called "edge", is labelled in green. Each multipoint thermocouple contains 6 separate thermocouples with a 0.5 mm diameter, which are soldered into a 3 mm protective sheath with a length of 3800 mm. The thermocouple tips are spaced 500 mm apart and the measurement points of each multipoint thermocouple are located vertically from the top of the 3000 mm long fins, starting at 250 mm from the top of the fins, with the sixth point located 2750 mm from the top and 250 mm from the bottom. The heights are: 250/750/1250/1750/2250/2750 mm.

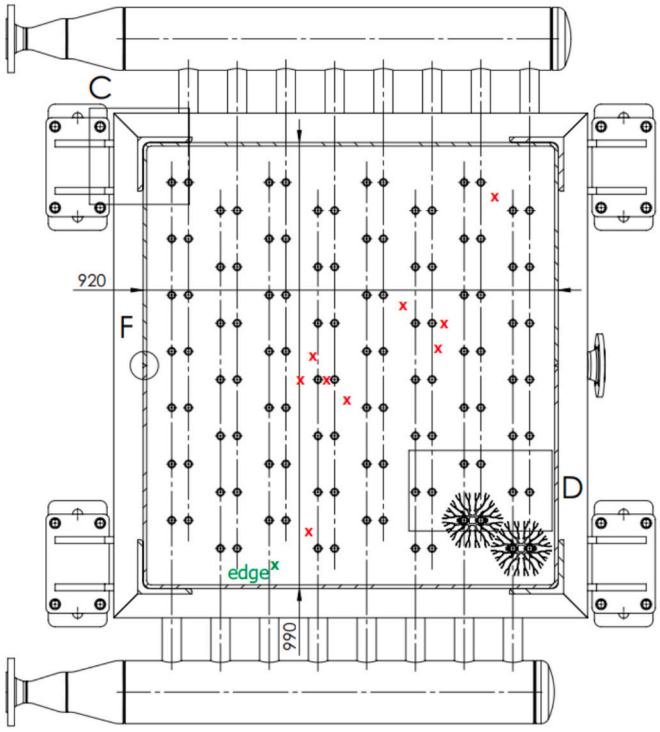

Fig. 4. Horizontal arrangement of the multipoint thermocouples in the LH-TES.

3. Methods

3.1. Heat balances and data reduction

As the LH-TES is used for condensation and evaporation of the refrigerant and the medium exiting the LH-TES may be in a two-phase flow, it is not possible to determine the heat flow rates directly from temperature differences at the inlet and outlet of the LH-TES. Thus, the different circuits of the test rig are used to determine the heat flow rates, as shown in Fig. 3.

For the charging process, the heat flow rate to the LH-TES $\dot{Q}_{LH(C)}$ (Eq. (1)) can be calculated based on the specific enthalpies at the LH-TES inlet and the condenser outlet and the heat flow rate dissipated by the oil circuit at the condenser $\dot{Q}_{con}$ (Eq. (2)). The refrigerant mass flow rate $\dot{m}_{ref(C)}$ is a direct measurement and the specific enthalpies $h_{ref,top}$ and $h_{ref,con}$ of the refrigerant can be determined with the pressures p and temperatures T at their specific positions and the fluid properties given by REFPROP [33]. For the calculation of the heat flow rate through the condenser $\dot{Q}_{con}$, the volumetric flow rate $\dot{V}_{oil}$ and the inlet and outlet temperatures $T_{oil,in}$ and $T_{oil,out}$ are measured. From these values, the temperature-dependent density ϱ and mean specific heat capacity $\bar{c}_{p,oil}$ are determined via a look-up table for the thermal oil Syltherm 800 [34].

$$\dot{Q}_{LH(C)} = \dot{m}_{ref(C)} \bullet \left[h_{ref,top}\left(p_{ref,top}, T_{ref,top}\right) - h_{ref,con}\left(p_{ref,con}, T_{ref,con}\right)\right] - \dot{Q}_{con} \tag{1}$$

$$\dot{Q}_{con} = \dot{V}_{oil} \bullet \varrho\left(T_{oil,in}\right) \cdot \bar{c}_{p,oil} \bullet \left(T_{oil,out} - T_{oil,in}\right) \tag{2}$$

For the discharging process, the heat flow rate from the LH-TES $\dot{Q}_{LH(D)}$ (Eq. (3)) can be calculated equivalently, but using the specific enthalpy $h_{ref,bot}$ at the bottom of the LH-TES and the mass flow rate $\dot{m}_{ref(D)}$.

$$-\dot{Q}_{LH(D)} = \dot{m}_{ref(D)} \bullet \left[h_{ref,bot}\left(p_{ref,top}, T_{ref,bot}\right) - h_{ref,con}\left(p_{ref,con}, T_{ref,con}\right)\right] - \dot{Q}_{con} \tag{3}$$

In the case of a sensible charging process of the LH-TES, the calculation of $\dot{Q}_{LH(C)}$ (Eq. (1)) could be simplified to $\dot{Q}_{LH(C),sens}$ (Eq. (4)).

$$\dot{Q}_{LH(C),sens} = \dot{m}_{ref(C)} \bullet \left[h_{ref,top}\left(p_{ref,top}, T_{ref,top}\right) - h_{ref,bot}\left(p_{ref,top}, T_{ref,bot}\right)\right] \tag{4}$$

The transferred heat Q in [kWh] can be calculated by the integral of the heat flow rates. Since the data are logged with a data acquisition time t, this integral can be rewritten as the sum of the calculated heat flow rate within the time period i multiplied by the data acquisition time t (Eq. (5)).

$$Q = \frac{\sum_{i=0}^{n} \dot{Q}_i \cdot t}{3600} \tag{5}$$

For the error calculation, Gaussian error propagation (see [35]) was applied (Eq. (6)), where k represents the considered equation, j its input arguments, σ_j the absolute error of the input argument and σ_k the absolute maximum error range of the calculated value of the equation. By the ratio of the absolute maximum error range to the considered value, the relative maximum error range ε_k (Eq. (7)) is obtained.

$$\sigma_k = \sqrt{\left(\frac{\partial k}{\partial j_1} \cdot s_{j1}\right)^2 + \left(\frac{\partial k}{\partial j_2} \cdot s_{j2}\right)^2 + \ldots} \tag{6}$$

$$\varepsilon_k = \frac{s_k}{k} \cdot 100 \tag{7}$$

3.2. Experimental parameters and procedures

This publication focuses on the transient discharging process. The LH-TES was experimentally analysed during a discharging process (D) in five test series (TS) with a nearly constant mass flow rate, except in TS1. Table 3 provides an overview of the experimental test campaign. To characterise the initial state of charge, the arithmetically averaged PCM temperature (mean PCM temperature) at the beginning of the experiments $T_{PCM,mean,ini}$ and the PCM edge temperature $T_{PCM,edge,ini}$ are given. The mean PCM temperature is calculated using the measured temperatures from the middle four temperature levels of the nine multipoint thermocouples marked in red in Fig. 4 (excluding the upper and lower thermocouple levels to avoid edge effects), resulting in a mean value calculated from 36 measured values. The PCM edge temperature is calculated from 4 measured temperatures from the edge multipoint thermocouple, marked in green in Fig. 4, again without the upper and lower measurement levels. This is to provide information on the LH-TES charge level and enable better comparability between the experiments. The listed refrigerant mass flow rates and temperatures are setpoint values. The system pressures between 11.4 bar at 104 °C and 18.7 bar at 129 °C result from the saturation pressure of the setpoint of the condenser temperature $T_{ref,con}$. During the discharge process, the feed pump slightly increases the pressure of the refrigerant for circulation by approx. 0.3–1.0 bar, depending on the setpoint of the mass flow rate. The measured resulting LH-TES inlet temperatures $T_{ref,bot}$ are about 1 K higher than the condenser setpoint temperatures $T_{ref,con}$, which are listed in Table 3.

With TS1 test series, the heat losses of the LH-TES were determined using the charging cycle (C). The heat balances to determine the heat losses can only be carried out using a combination of a system balance (Eq. (1)) on the fluid side and the energy balance of the condenser thermal oil circuit (Eq. (2)) with the LH-TES at a quasi-steady-state, using the temperature difference between the inlet and the outlet temperatures of the condenser thermal oil circuit. This calculation results in a high maximum error range.

To reduce the maximum error range, it is appropriate to determine the heat losses with sensitive heat transfer on the fluid side (Eq. (4)). For this purpose, the LH-TES was heated in the charging mode to a setpoint temperature and kept constant for around 48 h to achieve a quasi-

Table 3
Overview of the experimental parameters.

TS	Purpose	Exp.	Mode	$T_{PCM,mean,ini}$ [°C]	$T_{PCM,edge,ini}$ [°C]	$\dot{m}_{ref}$ [kg/s]	$T_{ref,con}$ [°C]
1	Heat loss determination	1.1	C	115.1	109.5	var.	var.
		1.2	C	125.2	118.7	var.	var.
		1.3	C	140.9	139.6	var.	var.
		1.4	C	145.4	144.2	var.	var.
2	Repeatability	2.1	D	139.1	139.8	0.6	114
		2.2	D	139.2	139.8	0.6	114
		2.3	D	139.1	128.4	0.6	114
3	Mass flow rate variation	3.1	D	139.0	125.1	0.3	114
		3.2	D	138.9	127.8	0.4	114
		3.3	D	138.7	127.4	0.5	114
		3.4	D	139.1	126.1	0.7	114
4	Evaporation temperature variation	4.1	D	138.6	125.6	0.6	104
		4.2	D	139.1	126.7	0.6	109
		4.3	D	138.8	126.3	0.6	119
		4.4	D	137.8	126.1	0.6	124
		4.5	D	137.3	127.3	0.6	129
5	Sequential and partial discharge	5	D	138.3	129.2	0.4	114

steady-state. This results in a state in which the test rig transfers the heat flow rate required to compensate for the LH-TES heat losses. The temperature values were then recorded for approximately 1 h and averaged over this period.

TS2 through TS5 analyse different experimental parameters. TS2 consists of three experiments in the upper mass flow rate range that were carried out with the same parameters at different dates to confirm the repeatability of the experimental procedure. To investigate the influence of the mass flow rate, the mass flow rates in TS3 were varied between 0.3 and 0.7 kg/s, which represents values between the upper and lower limits of the test rig, while keeping the LH-TES evaporation temperature constant at 114 °C. The influence of the evaporation temperature was investigated in the TS4 test series by varying the condenser temperature between 104 and 129 °C, which represents values for possible discharging scenarios with a 4 to 29 K temperature difference to the theoretical phase change temperature at a constant mass flow rate of 0.6 kg/s. Due to the large amount of refrigerant in the condenser, the condenser temperature determines the system pressure and thus the evaporation temperature. For TS5, the discharging process was sequentially interrupted to simulate a scenario of demand-driven heat utilisation.

A data recording interval of 0.07 Hz was selected for the experimental procedure. Before starting the discharging process, the LH-TES was fully charged and conditioned and kept constant to the setpoint temperature to enable temperature homogenisation processes within the PCM. Except for in the TS1 test series, the charging temperature was set to 143 °C in all experiments, which represents the upper temperature range of the test rig and which is 10 K above the theoretical phase change temperature of 133 °C. Since the test rig first starts internal conditioning when switching from charging to discharging mode before the LH-TES is integrated into its circuit, the starting point of the experiments needs to be defined. The first 0.2 to 1.0 h after the start of the discharging process was removed during data reduction as the processes strongly depend on the test rig control algorithm. This allows for comparability of the experiments, but in consequence, not the entire discharge capacity is included in the analysis. For example, the mean PCM temperature at the beginning of the discharging process in TS3 and TS4 was about 142 °C, but the analyses start at approximately 139 °C. The analyses for TS3, TS4 and TS5 start with the first increasing value of the heat flow rate, which represents 90 % of the maximum heat flow rate in the range of the heat flow rate plateau. The beginning of TS2.3 was also determined based on this criterion, while the other two experiments from TS2 were matched with the mean PCM temperature.

As this work focusses on the discharge cycle, no explicit round-trip efficiency is calculated for the storage within this work. On the one hand, the energy balance during the charging cycle would lead to a high maximum error, as mentioned above. On the other hand, the round-trip efficiency of the storage system is strongly influenced by the process in which the storage system is integrated, as this process defines the specific input and output requirements. In [25], the efficiency of this storage system when integrated into a Carnot battery has been estimated.

4. Experimental results and discussion

4.1. Heat losses, experimental repeatability and error range

The calculated heat losses $\dot{Q}_{LH,loss}$ for the four experiments from TS1 are plotted in Fig. 5. The average ambient temperature T_{Am} for all four experiments was 24 °C. As can be seen, the heat losses increase from 1.74 to 2.54 kW with increasing mean PCM temperature, whereby the relative maximum error ranges of the heat losses are between 1.8 and 3.0 %. The PCM edge temperature (Table 3) is critical for the analysis of heat loss, because this temperature forms the relevant difference to the ambient temperature. In the two experiments below the phase change range, Exp.1.1 and Exp.1.2, the edge temperature value is around 5 K below the mean PCM temperature, while in the two experiments above the melting range, Exp.1.3 and Exp.1.4, it is approximately the same. This is mainly due to an improved temperature homogenisation in the PCM in the liquid state due to natural convection.

To confirm the repeatability of the operating conditions, the actual values of the parameters mass flow rate and inlet temperature of the refrigerant into the LH-TES for the three experiments of TS2 with the

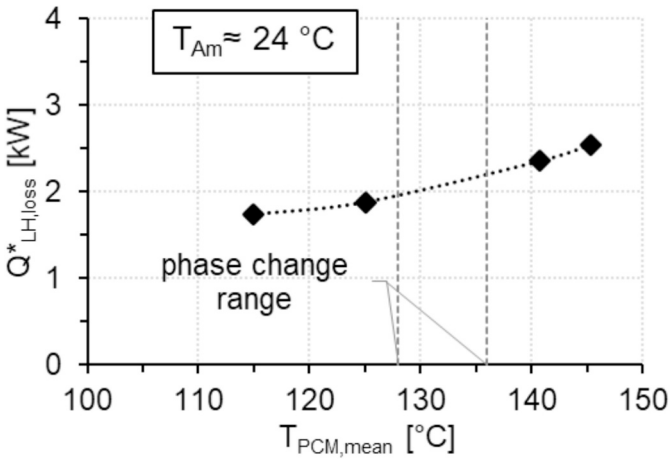

Fig. 5. TS1 – Heat losses of the LH-TES for different mean PCM temperatures.

same parameter settings are shown in Fig. 6 over the duration of the discharging process. As can be seen, the values are similar, verifying the repeatability of the setpoint parameters controlled by the test rig. The LH-TES inlet temperatures are close to the setpoint value of 114 °C over the entire period, whereas the mass flow rates are regulated to reach the target value of 0.6 kg/s during the duration of the discharging process. At the beginning of the discharging process, a slight deviation of the mass flow rate from Exp.2.3 can be recognised, which is due to the different starting conditions of the discharging process compared to the other two experiments. In Exp.2.3, the discharging process started with a PCM edge temperature of 10 K below the mean PCM temperature, while the discharging process in Exp.2.1 and Exp.2.2 started with a PCM edge temperature equal to the mean PCM temperature (Table 3). Because of this, the Exp.2.1 and Exp.2.2 analyses start at a later stage of the discharging processes, in order to match the experiments by using the mean PCM temperature of approximately 139.1 °C.

Since the test procedure in all further experiments corresponds to that of Exp.2.3 with a PCM edge temperature between 125.1 and 129.2 °C, Exp.2.3 is used as a reference experiment for further analysis. The pressure on the fluid side is not discussed in the following analysis, as it essentially depends on the temperature setpoint in the test rig condenser and remains almost constant over the entire duration of the discharging process.

To characterise the LH-TES performance, the calculated heat flow rate over the duration of the discharging process is shown in Fig. 7, with the corresponding maximum heat flow rates and transferred heat after 3 h and 4 h listed in Table 4. The profiles of the heat flow rates also confirm the experimental repeatability, where the small deviation from Exp.2.3 in the first 0.25 h is a result of the deviation of the mass flow rate shown in Fig. 6. Furthermore, the maximum heat flow rates in the selected parameter configuration for all experiments from TS2 are around 82 kW and thus also indicate repeatability of the discharging process. Within the first hour of the discharging process, it can be recognised that a plateau with an almost constant heat flow rate occurs, which can be explained by the solidification front moving from the bottom to the top of the LH-TES until reaching the top when the plateau ends. From this point onwards, the heat transfer surface between the working fluid and the storage material is completely covered with a growing layer of solidified PCM, which increases the heat transfer resistance and thus decreases the storage power. The heat flow rate drops steadily and approaches a mean value of 2.3 kW after 3 h and a mean value of 1.3 kW after 4 h for TS2, thus reaching values within the heat loss range. The TS2 mean value of the transferred heat after 3 h is 110.3 kWh and after 4 h is 112.1 kWh. Due to the small amount of heat transferred in this period, the discharging process can be considered almost complete after 3 h. The transferred heat of Exp.2.3 after 3 h is lower than in the other two TS2 experiments, by about 3.1 and 5.5 kWh,

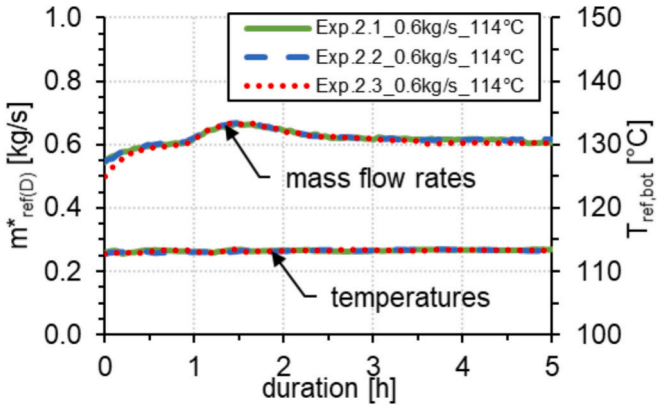

Fig. 6. TS2 – Verification of experimental repeatability based on the refrigerant mass flow rate and the LH-TES inlet temperature.

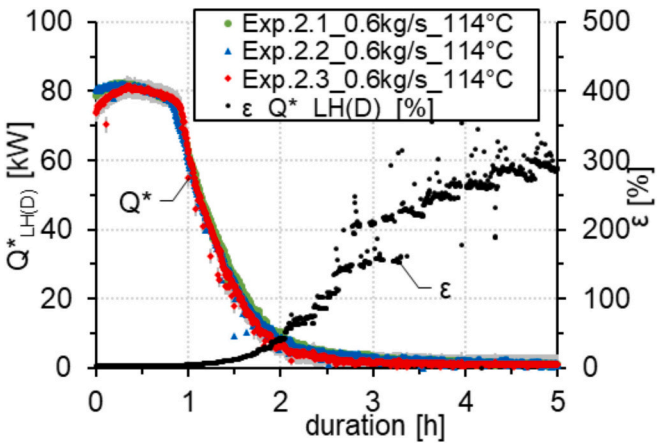

Fig. 7. TS2 – Calculated heat flow rates for TS2 and maximum error range shown for Exp.2.3.

Table 4
TS2 – Maximum heat flow rate and transferred heat after 3 and 4 h.

Exp.	$\dot{Q}_{max}$ [kW]	Q_{3h} [kWh]	Q_{4h} [kWh]
2.1	82.43	112.89	115.04
2.2	82.25	110.48	112.68
2.3	81.59	107.38	108.60

or 3 and 5 % less compared to the mean value. This is due to the share of heat stored in the PCM at the edge of the LH-TES, represented by higher PCM edge temperatures in Exp.2.1 and Exp.2.2 (Table 3).

As an example, the absolute maximum error range is plotted in grey bars and the relative maximum error range in black dots for Exp.2.3. The Gaussian error propagation method was used to calculate the maximum error range. In addition to the accuracies of the measuring devices given in Table 2, an accuracy of 1 % was also assumed for the fluid properties density and isobaric heat capacity of the thermal oil. The absolute maximum error range shown in grey for Exp.2.3 ranges between 1.5 and 2.9 kWh. Since the absolute error bars turn out to be small, they are hard to recognize. The heat flow rate at the condenser (Eq. (2)) has the highest share of the total error of the heat flow rate, whereby the inlet and outlet temperatures of the thermal oil have the greatest influence on it. The relative maximum error range shown with black dots is at an arithmetic mean of 3.4 % in the area of the heat flow rate plateau and increases with decreasing heat flow rate up to values of around 300 % for a discharging process duration of 5 h. With values of around 200 % at 3 h, this method is not suitable for the accurate determination of heat losses due to the high level of uncertainty. Nevertheless, the results depicted in Fig. 5 show that the heat flow rate values after a discharging process duration of 3 h are similar to the determined values of the heat losses. This confirms the order of magnitude of the heat losses using two different determination methods.

4.2. *Effect of mass flow rate variation*

Fig. 8 shows the results of the TS3 test series for the investigation of the influence of the mass flow rate on the characteristics of the discharging process; above are the heat flow rates and below the transferred heat plotted over the discharging process duration. The maximum heat flow rates decrease with decreasing mass flow rate, while the duration of the heat flow rate plateaus increases. This shows that the storage power is not limited by the dual tube heat exchanger, but by the mass flow rate of the working fluid. With higher mass flow rates, higher power rates and a faster discharging process can be achieved. In all experiments of TS3, the discharge process can be considered completed

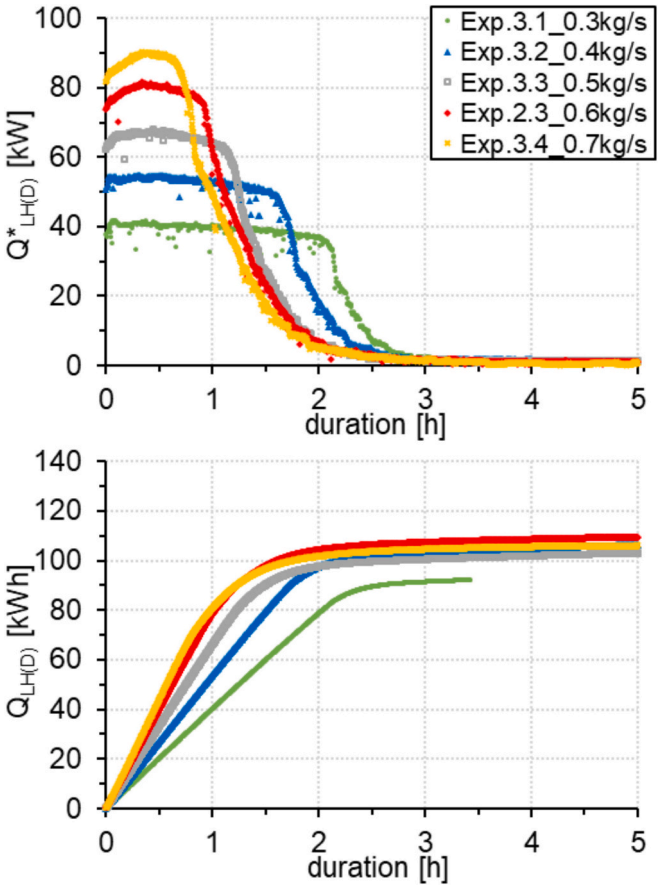

Fig. 8. Mass flow rate variation (TS3) – Heat flow rate (above) and transferred heat (below) for different mass flow rates.

after about 3 h. The diagram below shows that in all experiments, except Exp.3.1, the transferred heat is approximately 105 kWh. The transferred heat increases linearly during the duration of the heat flow rate plateau and continues to increase logarithmically when the sensible heat transfer dominates until its limit value is reached and the LH-TES can be considered completely discharged. The further slight increase of the transferred heat after a discharging process duration of 3 h can mainly be attributed to the compensation of the LH-TES heat losses.

In Exp.3.1 with the smallest mass flow rate of 0.3 kg/s, the analysis was stopped after about 3.5 h, because the specific enthalpy at the LH-TES inlet could no longer be determined in some time periods. In this experiment, the transferred heat of approximately 105 kWh was not achieved. This may be due to the low mass flow rate, leading to an uneven flow distribution in the 56 tubes. As a result, the heat stored in some areas of the PCM might not be dissipated. At the beginning of Exp.3.1, the calculated cross-sectional average speed of the refrigerant is 0.04 m/s in the liquid phase at the LH-TES inlet and 0.58 m/s in the gaseous phase at the LH-TES outlet. These are low values compared to typical values for shell-and-tube heat exchangers of 0.9 to 2.4 m/s [36]. To increase the transferred heat using such small mass flow rates, a different header design would be necessary.

For a quantitative comparison of the experiments, various performance parameters were defined and determined in Table 5. These are the test series TS3 experiments and include TS2 Exp.2.3 in order to have a consistent step size in the mass flow rate (see Table 3). The first parameter is the maximum heat flow rate $\dot{Q}_{max}$, which is defined by the maximum value of the heat flow rate transferred between the storage and the refrigerant. To be able to quantitatively describe the length of the heat flow rate plateau, the duration in which the heat flow rate was within a range of 90 % of its maximum value $dur\left(\dot{Q}_{90\%}\right)$ was determined with the transferred heat during this period $Q\left(\dot{Q}_{90\%}\right)$. As the biggest part of the discharging process was already completed after 3 h, visible in Fig. 8, the transferred heat for this discharging process duration Q_{3h} is listed. Using the reference experiment TS2 Exp.2.3 as the reference value for transferred heat after 3 h (107.4 kWh), the durations for reaching 50 % of this value $dur(Q_{50\%})$ and 80 % of this value $dur(Q_{80\%})$ were determined. During a period in which the heat flow rate is within 90 % of its maximum value, a heat between 64.2 and 83.3 kWh is transferred. The remaining share, between 19.3 and 41.4 kWh, relate to the 3 h discharging process duration, may be mainly attributed to the sensible heat share.

The performance parameters are visualised in Fig. 9 with the maximum heat flow rate and the discharging process duration over the mass flow rate set value. The empty symbols indicate heat flow rates and the full symbols durations. As shown, the maximum heat flow rate (black empty diamonds) is proportional to the mass flow rate, as expected. The duration of the heat flow rate plateau on the other hand is not directly anti-proportional to the mass flow rate. When the mass flow rate is increased by a certain factor, the duration is decreased by more

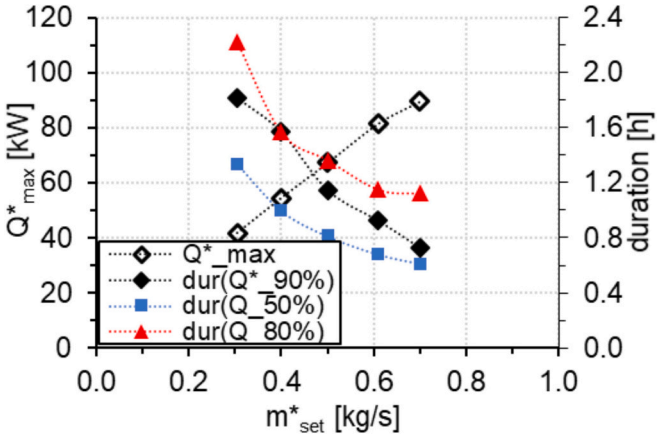

Fig. 9. Comparison of maximum heat flow rate and duration for different operating points over the mass flow rate setpoint.

Table 5
Mass flow rate variation (TS3 and TS2.3) – Mass flow rate, maximum heat flow rate, transferred heat during the heat flow rate plateau, duration of the plateau, transferred heat after 3 h and duration for reaching 50 and 80 % of this value.

Exp.	$\dot{m}$ [kg/s]	$\dot{Q}_{max}$ [kW]	$Q\left(\dot{Q}_{90\%}\right)$ [kWh]	$dur\left(\dot{Q}_{90\%}\right)$ [h]	Q_{3h} [kWh]	$dur(Q_{50\%})$ [h]	$dur(Q_{80\%})$ [h]
3.1	0.3	41.66	72.12	1.82	91.46	1.34	2.23
3.2	0.4	54.47	83.33	1.58	103.36	1.00	1.57
3.3	0.5	67.20	75.49	1.15	100.50	0.81	1.37
2.3	0.6	81.59	73.24	0.93	107.38	0.68	1.15
3.4	0.7	89.61	64.22	0.73	104.59	0.61	1.12

than that factor. This indicates higher discharge depths for smaller mass flow rates. The observation can be explained by the axial nature of the discharging process with small mass flow rates: Since the storage volume is discharged more slowly from bottom to top and it takes longer for the heat transfer surface between the working medium and the storage material to be completely covered by an insulating layer of solidified PCM, the performance of the heat exchanger is sufficient over a longer period of time. The mass flow rate therefore directly enables setting the heat flow rate and thus indirectly extending the discharging time according to the required conditions. Furthermore, the heat flow rate of 0.7 kg/s in Exp.3.4 deviates slightly from the proportionality, which could indicate that an upper heat flow rate limit of the LH-TES has been reached. This means that the heat flow rate cannot be increased by increasing the mass flow rate of the refrigerant, because the heat transfer resistance on the storage side dominates the overall heat transfer, as discussed in Dietz et al. [24]. In general, this tends to occur for high mass flow rates of the refrigerant and high radial heat transfer resistances in the storage and indicates that either the driving temperature difference between the PCM and the refrigerant is too low or the heat transfer enhancement by the fin is too weak for sufficient heat transfer. For this case, the heat flow rate does not show a heat flow rate plateau, but rather a heat flow rate peak (Fig. 8). The discharging process duration to discharge the LH-TES by 50 % (of the reference heat transfer value determined in Exp.2.3) (blue squares) and 80 % (red triangles), measured at the transferred heat at 0.6 kg/s (Exp.2.3) after 3 h is approximately exponential to the mass flow rate and decreases with increasing mass flow rate. The duration for the 50 % and 80 % discharging process between 0.6 kg/s (Exp.2.3) and 0.7 kg/s (Exp.3.4) decreases only slightly, which may also indicate an operating limit of this LH-TES.

In Fig. 10, the refrigerant outlet temperature of the LH-TES is plotted over the discharging process duration for the mass flow variations. In addition, the saturated temperature for the refrigerant pressure at the top of the LH-TES is plotted as a black line for Exp.2.3. Temperatures above the saturated temperature therefore indicate refrigerant superheating. For temperatures close to or below the saturated temperature, the vapour quality cannot be determined and is therefore unknown. The results show that the duration of superheated vapour decreases with increasing mass flow rate. The vapour in Exp.3.1 is overheated for about 2.1 h and in Exp.3.4 for about 0.7 h. During the discharging process, the evaporation zone of the refrigerant moves from the bottom to the top. On the PCM side, the phase change front in the PCM also moves in a longitudinal direction from the bottom to the top. As a result, the tube length downstream of the evaporation zone in which the vapour can be superheated decreases as the discharging process duration increases. It should be noted that the heat transfer coefficient in the evaporation zone is greater than in the sensitive heat transfer zone with superheated vapour. The vapour superheating ends at a duration at which the PCM phase change front reaches the upper end of the LH-TES, which is represented by the end of the heat flow rate plateau. The duration of vapour superheating can be extended by controlling the mass flow rate, but with the consequence of a decreasing heat flow rate.

The mean temperatures for each cross section were determined for Fig. 11 to investigate the longitudinal temperature distribution in the LH-TES at four heights, except for the PCM edge temperature and the upper and lower levels to avoid the influence of edge effects. Thus, each longitudinal mean temperature represents the arithmetic mean of nine temperature measurement positions in the cross section. The approximate PCM phase change range is shown in grey dashed lines and was estimated qualitatively by short-term plateaus in the temperature measurements in the PCM. The mean PCM temperature is shown as a black line. In the upper diagram of Fig. 11, Exp.3.2 was chosen to represent a low mass flow rate and in the lower diagram, Exp.3.4 was chosen to represent a high mass flow rate. At around 136 °C, the start of solidification is characterised by a dip in the discharging temperature profiles measured in the PCM. At 128 °C, the end of solidification is implied by a slight kink in the temperature profile. Overall, the longitudinal temperature spread in Exp.3.2 with a low mass flow rate is significantly higher than in Exp.3.4, with a high mass flow rate. This shows that at low mass flow rates, a longitudinal discharge of the LH-TES occurs and the solidification front predominantly follows the longitudinal direction, whereas at high mass flow rates, this discharging characteristic is less pronounced. At higher mass flow rates, the solidification front is expected to move predominantly in a radial direction, according to the numerical results of Dietz et al. [24].

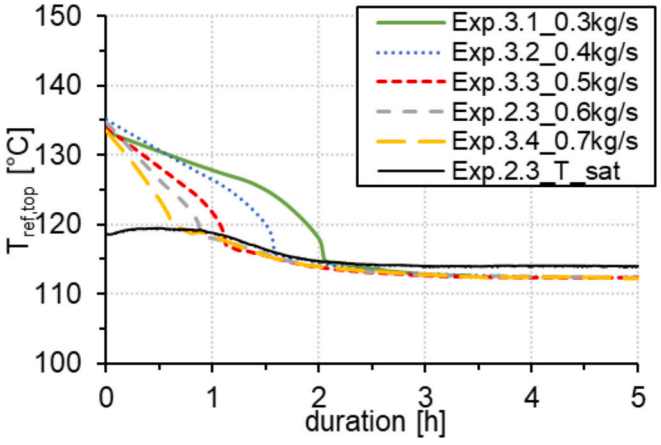

Fig. 10. Mass flow rate variation – LH-TES outlet temperature and saturated temperature (black line) for different mass flow rates.

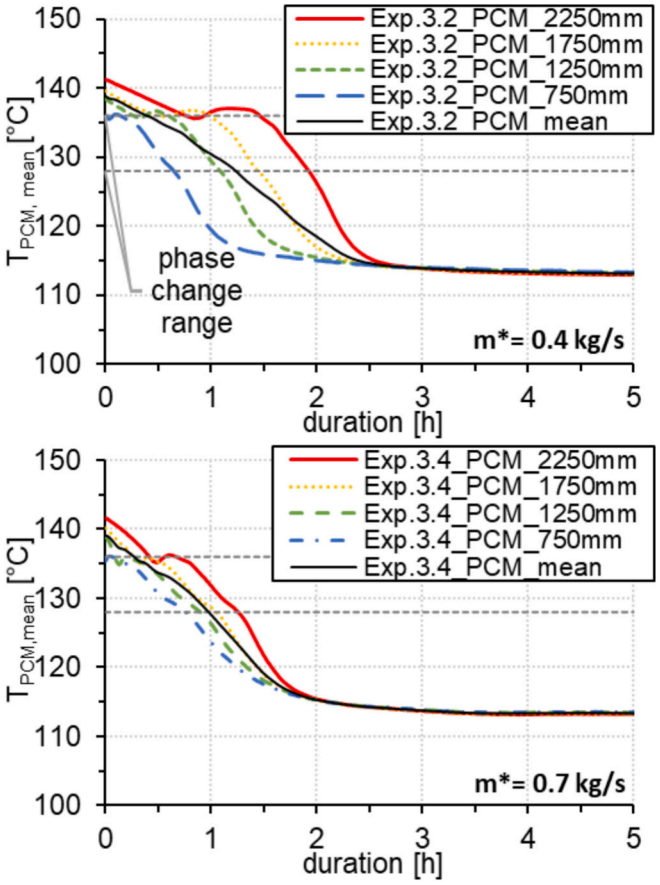

Fig. 11. Comparison of low and high mass flow rates – Temperature distribution at different LH-TES heights and mean PCM temperature (black line) for Exp.3.2 (above) and Exp.3.4 (below).

4.3. Effect of evaporation temperature variation

Fig. 12 shows the results of the investigation of the effect of the evaporation temperature on the characteristics of the discharging process, including the test series TS4 and the reference experiment Exp.2.3. Above are the heat flow rates and below the transferred heats are plotted over the discharging process duration. For the experiments with an evaporation temperature between 104 and 114 °C, the heat flow rate plateau has approximately the same duration, while in the experiments with an evaporation temperature between 119 and 129 °C, the duration decreases more strongly due to the decreasing driving temperature differences between the working medium and the PCM. For the same reason, the maximum heat flow rates decrease from about 90 kW for an evaporation temperature of 104 °C to about 60 kW for an evaporation temperature of 129 °C. Except for Exp.4.5, which shows rather a peak than a heat flow rate plateau, the variation of the evaporation temperature experiments can be considered fully discharged after 3 h. In Exp.4.5, the evaporation temperature of 129 °C is within the phase change range, which means that the solidification of the PCM is not fully completed. This is also visible in the transferred energies in the diagram at the bottom of Fig. 12. Here, the trend of the transferred heat of Exp.4.5 is not logarithmic but rather exponential. The maximum transferred heat decreases (from Exp.4.1 to Exp.4.5) with increasing evaporation temperature and thus decreasing sensible share. The numerical values can be seen in Table 6. For a 3 h discharging process duration, the transferred heat decreases from approximately 121.6 to 63.8 kWh with increasing evaporation temperature. The theoretical value for the sensible heat share of the PCM is 9.5 kWh for a temperature difference of 5 K. The real differences in the transferred heat in the experiments result in values between 2.0 and 21.9 kWh with a mean value of 11.6 kWh for a 3 h discharging process duration. The transferred heat of Exp.2.3 is close to that of Exp.4.2. This can be attributed to the method used to determine the starting point of the experimental analysis at the first increasing value of the heat flow rate. This represents 90 % of the maximum heat flow rate in the range of the heat flow rate plateau. Table 5 shows that the transferred heat at an evaporation temperature of 114 °C is approximately between 100.5 and 107.6 kWh. Exp.2.3 thus represents an upper outlier. Considering the heat flow rate plateau duration and the maximum heat flow rate, Exp.4.1, Exp.4.2 and Ex.2.3 show the most favourable characteristics. If the sensitive share of the transferred heat should be minimised, an evaporation temperature of 114 °C is preferable for this investigated LH-TES.

Table 6
Variation in evaporation temperature – Condenser setpoint temperature, maximum heat flow rate, duration of the heat flow rate plateau and transferred heat after 3 and 4 h.

Exp.	$T_{ref.con}$ [°C]	$\dot{Q}_{max}$ [kW]	$dur\left(\dot{Q}_{90\%}\right)$ [h]	Q_{3h} [kWh]	Q_{4h} [kWh]
4.1	104	90.37	1.00	121.57	123.78
4.2	109	85.25	0.97	109.54	110.78
2.3	114	81.59	0.93	107.58	108.84
4.3	119	74.55	0.63	85.66	87.13
4.4	124	67.53	0.33	69.60	71.63
4.5	129	58.11	0.15	63.77	68.44

The refrigerant pressure measured at the top of the LH-TES is shown in Fig. 13. All pressures adapt to the saturation pressure during the discharging process according to the temperature setpoint for the test rig condenser. In the beginning, these pressures deviate slightly, as the

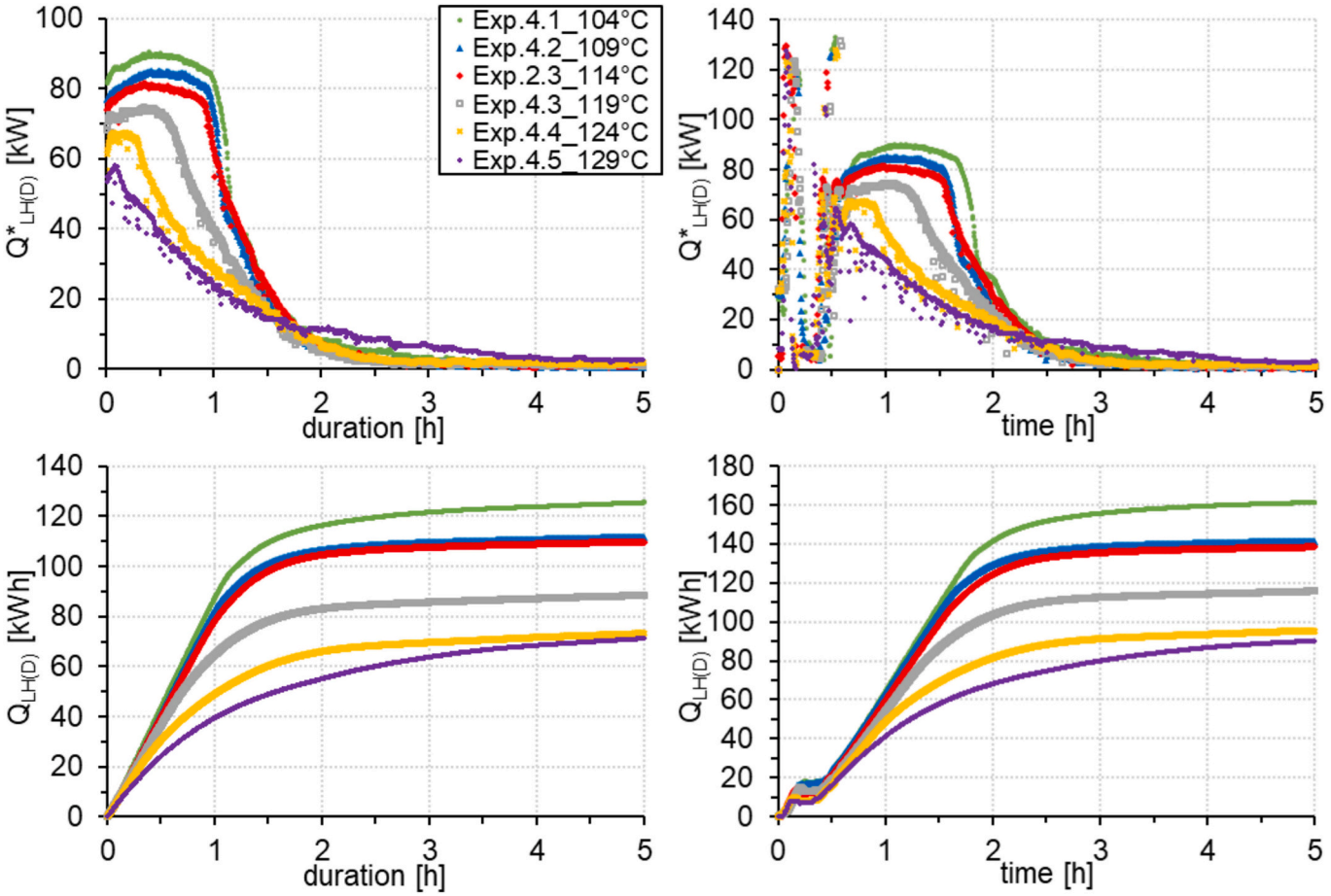

Fig. 12. Variation in evaporation temperature – heat flow rate (above) and transferred heat (below) for different discharging temperatures.

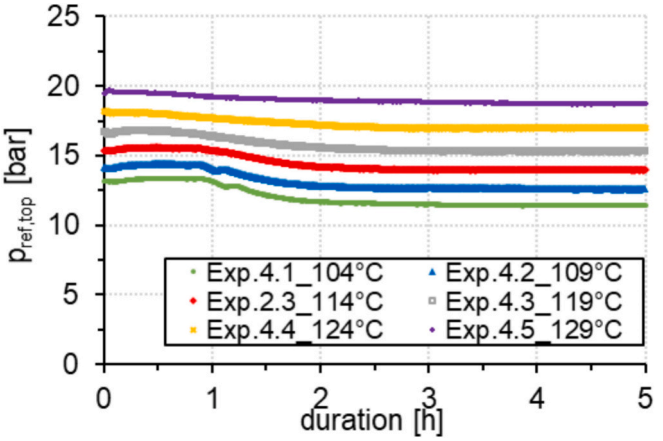

Fig. 13. Variation in evaporation temperature – LH-TES outlet pressures for different evaporation temperatures.

influence of the heat flow rate fed into the system via the LH-TES on the pressure dominates, while with increasing duration of the discharging process, the influence of the heat flow rate dissipated via the condenser on the system pressure predominates. Overall, the discharging process of the LH-TES with the test rig can be classified under the boundary conditions of constant mass flow rate and constant pressure, which shows great potential for more flexible operating strategies for storage integration in specific applications as proposed by Garcia et al. [25].

4.4. Sequential LH-TES discharging process

To experimentally simulate a scenario of demand-driven heat utilisation, the discharging process was interrupted sequentially (TS5 from Table 3). The mass flow rate was set to 0.4 kg/s and the condenser temperature to 114 °C, which correspond to the parameter settings of the reference experiment Exp.3.2. The results can be seen in Fig. 14, with the heat flow rate shown above and the transferred heat below. The sequences are divided as follows: 0.5 h discharge - 1 h break - 0.5 h discharge - 1 h break - complete discharge. During the breaks, the refrigerant was bypassed around the LH-TES. As can be seen from the fluctuations in the heat flow rate that are caused by mass flow rate fluctuations, the test rig control requires around 0.5 h to adjust to the mass flow rate setpoint. The heat flow rate plateau that occurs in the last discharging process sequence is of the same order of magnitude as in Exp.3.2, at around 50 kW. The LH-TES can be considered fully discharged after about 5 h. As in Exp.3.2, the sum of the discharge sequence durations until the LH-TES is completely discharged is around 3 h. After this period, at a discharging process duration of 5 h, the transferred heat is about 100.1 kWh, which is also in the same order of magnitude as the values given in Table 5. Furthermore, the fact that the transferred heat is not significantly higher than in the comparative experiments shows that the aluminium fins conduct the heat effectively in the radial direction and fully utilise the heat capacity of the PCM. The results show that the LH-TES can be flexibly discharged on demand with interruptions in the order of hours without sacrificing storage power or capacity, making it suitable for use as a steam generator in batch processes and therefore competitive with conventional steam generators in this respect.

Equivalent to Fig. 11, Fig. 15 shows the temperature distribution in the PCM for different LH-TES heights and the mean PCM temperature as a black line. After the first discharge sequence, solidification of the PCM has begun in the lower part of the LH-TES, while the PCM is still liquid in the middle and upper part of the LH-TES. In the second discharge sequence, the PCM is completely solidified in the lower part of the LH-TES, while PCM solidification begins in the middle part of the LH-TES and the PCM is still in a liquid state in the upper part of the LH-TES. At the end of the third and final discharge sequence, the PCM

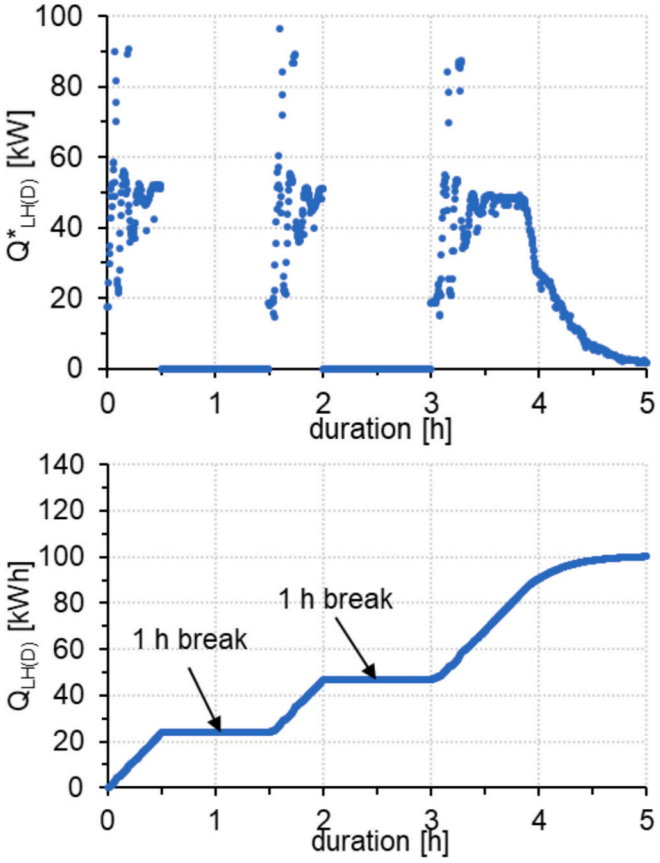

Fig. 14. Interruption of discharging (TS5) – Heat flow rate (above) and transferred heat (below) for a sequential discharging process scenario.

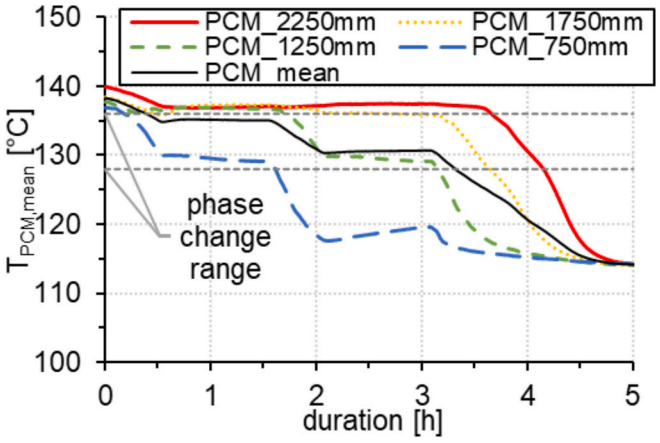

Fig. 15. Interruption of discharging (TS5) – PCM temperature distribution at different LH-TES heights and mean PCM temperature (black line) for a sequential discharging process scenario.

solidifies over the entire LH-TES height. It becomes apparent that the PCM temperatures gradually fall below the phase change range with a delay in each LH-TES height. In the second break sequence, between a discharging process duration of 2 to 3 h, the longitudinal mean PCM temperature at an LH-TES height of 750 mm undergoes a temperature homogenisation process and increases slightly. This is exclusively noticeable at this LH-TES height, as the solidification of the PCM is finished and the heat consumption due to temperature homogenisation processes is visible as a temperature increase. All other temperatures are above the lower phase change range and therefore do not show any

temperature increase during the break sequences. Overall, the longitudinal temperature levels in the LH-TES show that the solidification front in this parameter configuration moves from the bottom to the top of the LH-TES and that the selected times of the break sequences have no significant influence on the PCM phase stratification in the LH-TES.

4.5. Storage capacity discussion

As stated in the introduction, latent heat storage units are in part used due to their volumetric high energy density, and the storage capacity of a given unit is of critical importance. In this storage unit, a mixture of KNO_3 and $LiNO_3$ was used as the storage material. This PCM, as discussed in section 2.1, has a theoretical phase change enthalpy of between 160 and 170 kJ/kg and a specific isobaric heat capacity 1.17 kJ/(kgK) as stated in Milian et al. [32]. Using the conservative enthalpy of 160 kJ/kg and the fill amount of 4450 kg, the theoretical capacity of the LH-TES with this eutectic mixture at a temperature between 104 and 139 °C are 50.6 kWh of sensible heat and 197.8 kWh of latent heat, resulting in a total of 248.4 kWh. The maximum heat transferred and therefore stored energy in these experiments was measured in Exp.4.1 at 124 kWh, measured while cycling between 104 °C and 139 °C.

One of the reasons for the deviation of the theoretical values from the experimentally determined values is that the analysis of the discharge process starts at a later stage than the experiments. This is necessary to enable comparability between the experiments, but at the same time means heat quantities of approximately 25 to 30 kWh are not considered.

A further influence could be that, due to the non-eutectic PCM mixture, the actual phase change temperature is below the minimum discharge temperature or above the maximum charging temperature, so that the entire phase change enthalpy could not be fully utilised.

The PCM was analysed with direct scanning calorimetry (DSC) using a DSC 204 F1 Phoenix from Netzsch. Salt samples of around 10 mg were weighed in perforated and cold-pressed standard aluminium crucibles. An inert atmosphere of 40 mL/min nitrogen and a heating rate of 10 K/min was used. The DSC results from one of the measurements are shown in Fig. 16; the curves of the repeated measurements were very similar. The melting onset temperature was measured at 123.5 °C and ended at 142.6 °C, with the melting curve showing a double peak that could be attributed to the non-eutectic mixture; for solidification, the boundaries were measured at 111.8 °C and 101.1 °C. These measurements show that with the operating conditions possible with the system, neither a full charging nor a full discharging likely occurred in the testing.

Furthermore, edge effects also have an influence, i.e. areas in the storage cross-section (Fig. 4) that have no fin material due to fin and storage tank geometry; therefore, the usable phase change enthalpy of the PCM in these areas was limited. These areas account for around 9 % of the cross-sectional area.

5. Conclusions and outlook

In this paper, the experimental analysis of the discharging of a novel dual-tube latent heat storage unit is discussed. The dual-tube design allows for the independent charging and discharging of the storage medium, allowing for a flexible installation in processes with differing heat transfer fluid or parameters thereof. In this paper, the discharging is analysed using a dedicated test rig for operation. A eutectic KNO_3-$LiNO_3$ mixture with a phase change temperature of about 133 °C is the PCM and R1233zd(E) the heat transfer fluid. The results show good heat conduction into the storage unit. No significant improvement in the results is expected by using both instead of one of the tube systems.

The storage unit discharging was characterised by a variation in mass flow rates between 0.3 kg/s and 0.7 kg/s, indicating that mass flow rate control is well suited for adjusting the vapour superheating and maximum heat flow rate.

A variation in evaporation temperature between 109 °C and 129 °C showed an optimum at 114 °C for maximizing the latent heat plateau length, which is strongly influenced by the PCM.

In addition, the results of a sequential discharging process confirm the possibility of flexible LH-TES operation and thus a demand-orientated vapour supply.

The dual-tube longitudinal aluminium fins used in the LH-TES proved effective, so that future investigations can focus on cost-optimised fins and system integration. At low mass flow rates, the entire storage capacity could no longer be discharged, though the headers were also not designed for these operating conditions. For such low flow rates, a reduction in the tube diameter or the number of tubes could offer the potential for extending the lower LH-TES operating

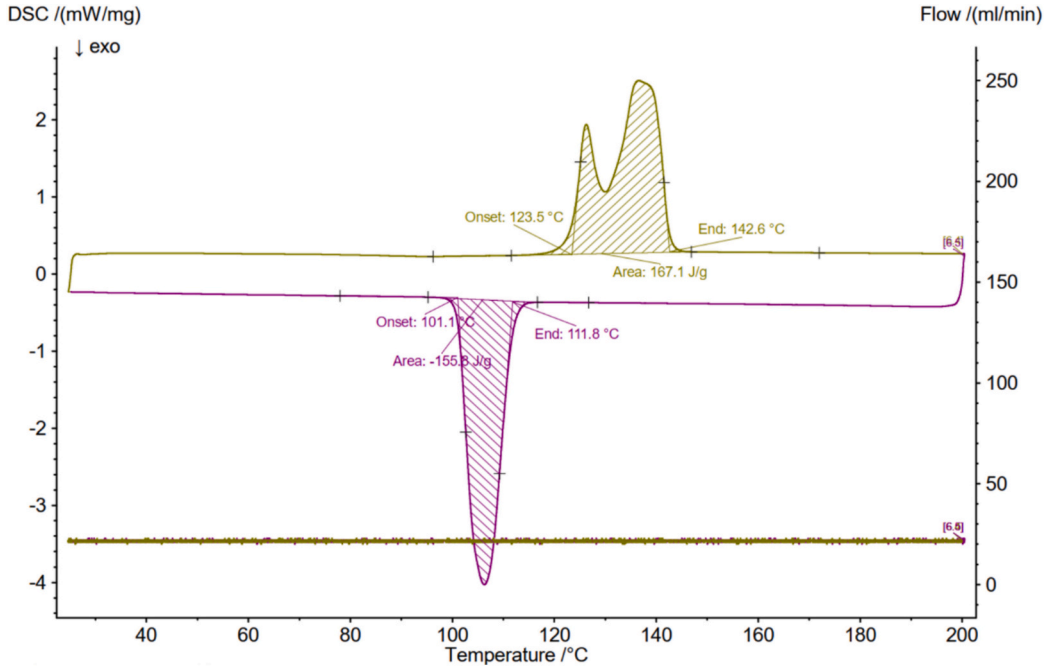

Fig. 16. DSC results for the technical grade PCM in the LH-TES.

range.

The PCM selected and analysed in this study was determined by constrictions in the system setup in [27]. A more economical PCM with a higher phase change temperature for process steam generation would increase overall feasibility, whereby this depends strongly on the heat source temperatures for the integration process. In the case of an electrical charging process, KNO_3-$NaNO_3$ with a phase change temperature of around 222 °C or $NaNO_3$ with a phase change temperature of around 306 °C would be preferable. In addition, when using eutectic mixtures, it is very important to have good literature data for the exact mixture of the components to ensure full functionality of the system and use of the latent heat capabilities.

This basic analysis shows the feasibility and flexibility of the novel dual-tube storage design. Further development for electrical charging and thermal discharging would make an integration in a system with no thermal source feasible. Further analysis of the influence of mass flow rate and pressure on the PCM melting and solidification would greatly strengthen the understanding and therefore design process for finned-tube storage units, therefore leading to more economical systems.

CRediT authorship contribution statement

K. Theologou: Writing – original draft, Visualization, Validation, Methodology, Investigation, Formal analysis, Data curation, Conceptualization. **L. Dietz:** Writing – review & editing, Validation, Methodology, Formal analysis, Data curation, Conceptualization. **J. Tombrink:** Writing – review & editing, Methodology, Conceptualization. **M. Johnson:** Writing – review & editing, Supervision, Project administration, Methodology, Funding acquisition.

Declaration of competing interest

The authors declare that they have no known competing financial interests or personal relationships that could have appeared to influence the work reported in this paper.

Acknowledgements

The work presented in this paper is a result of research activities of the CHESTER Project (www.chester-project.eu) which received funding from the European Union's Horizon 2020 research and innovation programme under grant agreement No 764042.

Data availability

Data will be made available on request.

References

[1] R. Jacob, M. Hoffmann, J.M. Weinand, J. Linßen, D. Stolten, M. Müller, The future role of thermal energy storage in 100% renewable electricity systems, Renewable and Sustainable Energy Transition 4 (2023), https://doi.org/10.1016/j.rset.2023.100059.

[2] G.P. Thiel, A.K. Stark, To decarbonize industry, we must decarbonize heat, in English, Joule 5 (3) (2021) 531–550. Mar 17, https://doi.org/10.1016/j.joule.2020.12.007.

[3] M.S. Ziegler, et al., Storage requirements and costs of shaping renewable energy toward grid decarbonization, Joule 3 (9) (2019) 2134–2153, https://doi.org/10.1016/j.joule.2019.06.012.

[4] K. Merlin, J. Soto, D. Delaunay, L. Traonvouez, Industrial waste heat recovery using an enhanced conductivity latent heat thermal energy storage, in English, Appl. Energy 183 (2016) 491–503. Dec 1, https://doi.org/10.1016/j.apenergy.2016.09.007.

[5] M. Johnson, M. Fiss, Superheated steam production from a large-scale latent heat storage system within a cogeneration plant, communications Engineering 2 (1) (2023), https://doi.org/10.1038/s44172-023-00120-0.

[6] V. Vuillerme, et al., Experimental results of 2018 Test campaign of the ALSOLEN 450 prototype for direct steam generation and thermal storage, in: AIP Conf. Proc 2303, 2020, p. 1, https://doi.org/10.1063/5.0028743.

[7] W.-D. Steinmann, Thermo-mechanical concepts for bulk energy storage, Renew. Sustain. Energy Rev. 75 (2017) 205–219, https://doi.org/10.1016/j.rser.2016.10.065.

[8] W.D. Steinmann, The CHEST (Compressed Heat Energy STorage) concept for facility scale thermo mechanical energy storage, Energy 69 (2014) 543–552, https://doi.org/10.1016/j.energy.2014.03.049.

[9] A. Vecchi, et al., Carnot Battery development: A review on system performance, applications and commercial state-of-the-art, J Energy Storage 55 (2022), https://doi.org/10.1016/j.est.2022.105782.

[10] O. Dumont, G.F. Frate, A. Pillai, S. Lecompte, M. De Paepe, V. Lemort, Carnot battery technology: a state-of-the-art review, J Energy Storage 32 (2020), https://doi.org/10.1016/j.est.2020.101756.

[11] W.-D. Steinmann, Thermal Energy Storage for Medium and High Temperatures: Concepts and Applications, Springer Fachmedien, Wiesbaden, 2022.

[12] Z.L. Yang, R. Walvekar, W.P. Wong, R.K. Sharma, S. Dharaskar, M. Khalid, Advances in phase change materials, heat transfer enhancement techniques, and their applications in thermal energy storage: A comprehensive review (in English), J. Energy Storage 87 (2024) 111329, https://doi.org/10.1016/j.est.2024.111329. May 15.

[13] X.L. Yu, et al., Synergistic improvement of melting rate and heat storage capacity by a rotation-based method for shell-and-tube latent thermal energy storage, in English, Appl. Therm. Eng. 219 (2023) 119480, https://doi.org/10.1016/j.applthermaleng.2022.119480. Jan 25.

[14] Z.H. Low, Z. Qin, F. Duan, A review of fin application for latent heat thermal energy storage enhancement, J Energy Storage 85 (2024), https://doi.org/10.1016/j.est.2024.111157.

[15] Q. Li, C. Li, Z. Du, F. Jiang, Y. Ding, A review of performance investigation and enhancement of shell and tube thermal energy storage device containing molten salt based phase change materials for medium and high temperature applications, Appl. Energy 255 (2019), https://doi.org/10.1016/j.apenergy.2019.113806.

[16] B.K. Choure, T. Alam, R. Kumar, A review on heat transfer enhancement techniques for PCM based thermal energy storage system, J Energy Storage 72 (2023), https://doi.org/10.1016/j.est.2023.108161.

[17] S. Zhang, S. Mancin, L. Pu, A review and prospective of fin design to improve heat transfer performance of latent thermal energy storage, J Energy Storage 62 (2023), https://doi.org/10.1016/j.est.2023.106825.

[18] F. Ren, et al., Study on thermal performance of a new optimized snowflake longitudinal fin in vertical latent heat storage, J Energy Storage 50 (2022), https://doi.org/10.1016/j.est.2022.104165.

[19] D. Laing, T. Bauer, N. Breidenbach, B. Hachmann, M. Johnson, Development of high temperature phase-change-material storages, Appl. Energy 109 (2013) 497–504, https://doi.org/10.1016/j.apenergy.2012.11.063.

[20] J. Vogel, M. Keller, M. Johnson, Numerical modeling of large-scale finned tube latent thermal energy storage systems, J Energy Storage 29 (2020), https://doi.org/10.1016/j.est.2020.101389.

[21] M. Johnson, J. Vogel, M. Hempel, B. Hachmann, A. Dengel, Design of high temperature thermal energy storage for high power levels, Sustain. Cities Soc. 35 (2017) 758–763, https://doi.org/10.1016/j.scs.2017.09.007.

[22] M. Johnson, et al., Assembly and attachment methods for extended aluminum fins onto steel tubes for high temperature latent heat storage units, Appl. Therm. Eng. 144 (2018) 96–105, https://doi.org/10.1016/j.applthermaleng.2018.08.035.

[23] P. Garcia, M. Olcese, S. Rougé, Experimental and numerical investigation of a pilot scale latent heat thermal energy storage for CSP power plant, Energy Procedia 69 (2015) 842–849, https://doi.org/10.1016/j.egypro.2015.03.102.

[24] L. Dietz, I. Bürger, A. Gutierrez, Effect of steam flow parameters on the partial load behaviour of a PCM storage, J Energy Storage 89 (2024), https://doi.org/10.1016/j.est.2024.111709.

[25] P. Garcia, G. Largiller, Performances and control aspects of steam storage systems with PCM: key learnings from a pilot-scale prototype, Appl. Energy 325 (2022), https://doi.org/10.1016/j.apenergy.2022.119817.

[26] "CHESTER - Compressed heat energy storage for energy from renewable sources." EU Horizon 2020 (grant agreement No. 764042). https://www.chester-project.eu/ (accessed 29 April, 2024).

[27] K. Theologou, et al., CHESTER: Experimental prototype of a compressed heat energy storage and management system for energy from renewable sources, Energ. Conver. Manage. 311 (2024), https://doi.org/10.1016/j.enconman.2024.118519.

[28] K. Couvreur, R. Tassenoy, X. van Heule, M. De Paepe, S. Lecompte, Experimental and numerical analysis of variable volume ratio as additional optimization parameter in organic Rankine cycle expanders, Appl. Therm. Eng. 216 (2022), https://doi.org/10.1016/j.applthermaleng.2022.119007.

[29] C. Arpagaus, F. Bless, M. Uhlmann, J. Schiffmann, S.S. Bertsch, High temperature heat pumps: market overview, state of the art, research status, refrigerants, and application potentials, Energy 152 (2018) 985–1010, https://doi.org/10.1016/j.energy.2018.03.166.

[30] M. Gueani, H. Zamali, M. Jimal, Diagramme de phases LiNO3-KNO3, Solid state chemistry and crystal chemistry (2) (1998) 787–789.

[31] R. Tamme, T. Bauer, J. Buschle, D. Laing, H. Müller-Steinhagen, W.-D. Steinmann, Latent heat storage above 120°C for applications in the industrial process heat sector and solar power generation, Int. J. Energy Res. 32 (3) (2008) 264–271, https://doi.org/10.1002/er.1346.

[32] Y.E. Milian, S. Ushak, L.F. Cabeza, M. Grageda, Advances in the development of latent heat storage materials based on inorganic lithium salts, Sol. Energy Mater. Sol. Cells 208 (2020), https://doi.org/10.1016/j.solmat.2019.110344.

[33] Reference Fluid Thermodynamik and Transport Properties (REFPROP). (2018). National Institute of Standards and Technology (NIST), Boulder, Colorado.
[34] Syltherm 800 - Heat Transfer Fluid - Product Technical Data, Trademark of the Dow Chemical Company, 1997.
[35] U. Ritgen, Gaussian error propagation, in: Analytical Chemistry II, Springer Berlin Heidelberg, Berlin, Heidelberg, 2025, pp. 235–243.
[36] T. Kuppan, Heat exchanger design handbook (Mechanical engineering, no. 126), Marcel Dekker, New York, 2000, pp. 232–1119.